J. Fluid Mech. (2012), *vol.* 696, *pp.* 215–227.
doi:10.1017/jfm.2012.27

A ratchet trap for Leidenfrost drops

Thomas R. Cousins, Raymond E. Goldstein†, Justin W. Jaworski and Adriana I. Pesci

Department of Applied Mathematics and Theoretical Physics, University of Cambridge, Wilberforce Road, Cambridge CB3 0WA, UK

(Received 25 August 2011; revised 23 December 2011; accepted 10 January 2012; first published online 27 February 2012)

The Leidenfrost effect occurs when a drop of liquid (or a sublimating solid) is levitated above a sufficiently hot surface through the action of an insulating vapour layer flowing from its bottom surface. When such a drop is levitated above a surface with parallel, asymmetric sawtooth-shaped ridges it is known to be propelled in a unique direction, or ratcheted, by the interaction of the vapour layer with the surface. Here we exploit this effect to construct a 'ratchet trap' for Leidenfrost drops: a surface with concentric circular ridges, each asymmetric in cross-section. A combination of experiment and theory is used to study the dynamics of drops in these traps, whose centre is a stable fixed point. Numerical analysis of the evaporating flows over a ratchet surface suggests new insights into the mechanism of motion rectification that are incorporated into the simplest equations of motion for ratchet-driven motion of a Leidenfrost body; these resemble a central force problem in celestial mechanics with mass loss and drag. A phase-plane analysis of experimental trajectories is used to extract more detailed information about the ratcheting phenomenon. Orbiting drops are found to exhibit substantial deformations; those with large internal angular momentum can even undergo binary fission. Such ratchet traps may thus prove useful in the controlled study of many properties of Leidenfrost drops.

Key words: condensation/evaporation, drops

1. Introduction

In 1756 Johann Gottlob Leidenfrost discovered that a drop of fluid placed on a sufficiently hot surface would not boil away immediately, but would instead levitate on a cushion of its own vapour and persist for a considerable time (Leidenfrost 1756). One of the notable properties of such Leidenfrost drops moving on smooth surfaces is their high-speed ballistic motion, ricocheting from one lateral boundary to another. Such motions make it difficult to study the radial flows and persistent shape oscillations of large drops (Adachi & Takaki 1984). It is therefore of interest to develop methods to confine these lateral motions, as Leidenfrost himself did with a heated spoon. A key modern breakthrough in the control of Leidenfrost drops was the discovery (Linke *et al.* 2006) that a surface with parallel asymmetric ridges will act as a ratchet, propelling the drops in the direction toward the steeper sides of the ridges, an effect that has been attributed to the flow features underneath deformed drops.

† Email address for correspondence: R.E.Goldstein@damtp.cam.ac.uk

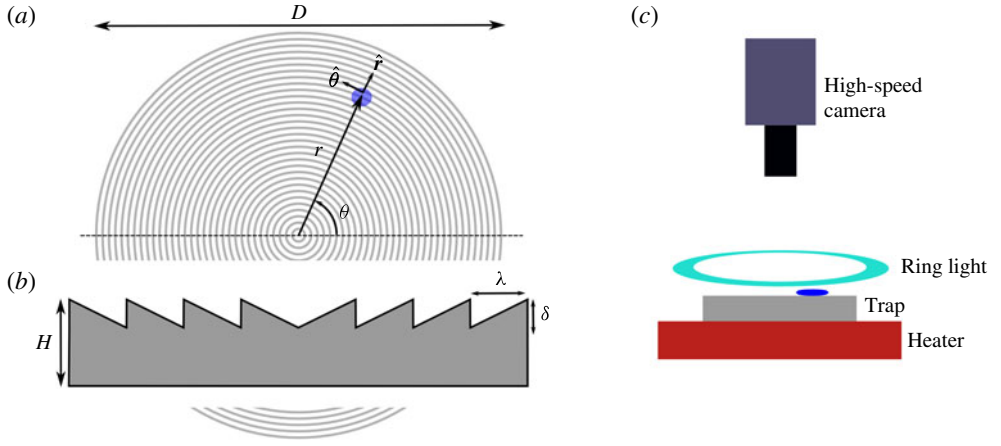

FIGURE 1. Experimental details. (*a*) The ratchet trap geometry and coordinate system for a moving drop (blue) at position $\boldsymbol{r} = (r, \theta)$ relative to the trap origin. (*b*) Side view of ratchet (not to scale), indicating the orientation of the teeth. (*c*) Experimental setup.

If such textured surfaces can 'rectify' the vapour flow from drops to produce unidirectional motion, then it is natural to ask whether there are modifications that might allow a drop to be coerced into moving along regular trajectories within a finite domain. Here we show that a surface textured with concentric circular ridges, each with a ratchet shape, acts as such a trap. In § 2 we describe the trap geometry and methods to determine drop trajectories, along with the basic experimental observations of drop orbits. We focus on the evolution of velocities and accelerations for quasi-one-dimensional trajectories, but also show that drops with large internal angular momentum can become unstable to binary fission. Numerical analysis of flows over a ratchet topography is used in § 3 to assess the original proposal of the ratcheting mechanism (Linke *et al.* 2006) and to reconcile it with more recent work (Dupeux *et al.* 2011*a*,*b*; Lagubeau *et al.* 2011), leading to the simplest drop equations of motion in § 4. The experimental results show systematic deviations from this simple model, and several possible mechanisms for this are suggested. We conclude by highlighting areas for further investigation.

2. Experimental methods and results

The trap shown schematically in figure 1 was machined from a block of aluminium to a height $H = 2$ cm and diameter $D = 15$ cm, surrounded by a raised lip 1 mm high to contain the drops. The ratchet pattern has a depth of $\delta = 0.3$ mm and a repeat distance $\lambda = 1.5$ mm. The orientation of the teeth shown in cross-section in figure 1(*b*) was chosen to drive drops toward the centre. Experiments were performed by heating the trap on a hot plate (Series 11–110, Fisher Scientific; 18 cm × 18 cm) to 300 °C (well within the 'Leidenfrost regime' for water), as determined by a contact thermometer (Amprobe/Meterman TPP2-C) on the disc. Drops were placed on the trap by slowly injecting water from a syringe through plastic tubing, the end of which was held a few millimetres above the trap surface. The drop is held by capillary forces at the end of the tubing and can be released from rest or with angular momentum relative to the trap centre by slowly dragging the drop laterally until released.

Drops were imaged with a high-speed video camera (Phantom V.1, Vision Research) suspended above the disc, operating at full frame resolution (1024 × 1024 pixels)

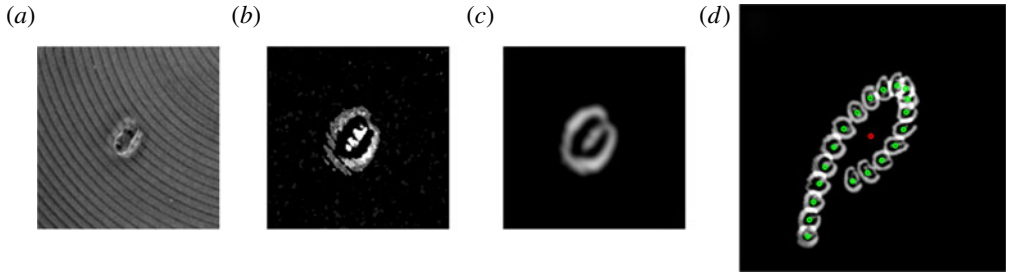

FIGURE 2. Image processing method. An image of the trap is subtracted from each raw video frame (*a*) to reveal (*b*) the halo produced around each drop from the ring light. (*c*) De-noising, bandpass filtering, and contrast enhancement yield a smoothed image suitable for accurate centroid detection. (*d*) A superimposed sequence of images 50 ms apart along an orbit, showing in green the detected centroids of each greyscale pattern and the trap centre (red).

at speeds of 200–1000 f.p.s., and equipped with an SLR lens (Nikon 50 mm f/1.4). The drops were illuminated with a 19 cm inner diameter 22 W fluorescent ring light (tube diameter 15 mm) concentric with the trap and slightly above it, as shown in figure 1(*c*), shielded to prevent glare. This lateral lighting creates a diffuse reflected halo around the drop which is easily visible by frame subtraction, as shown in figure 2. Appropriate filtering and de-noising of this greyscale pattern using ImageJ and Matlab enables accurate centroid detection to obtain the drop trajectory, despite the sometimes wild internal oscillations of the drop. The positional time series was processed with an algorithm based on a sliding window of many time steps, within which a least-squares fit of a high-order polynomial was used to smooth the data and obtain reliable time derivatives.

Drops of radius $R \sim 3$–5 mm released near the outer edge of the trap typically orbit for several seconds and always reach the trap centre before disappearing through vaporisation. There are two main types of trajectories distinguished by the magnitude of their initial orbital angular momentum. Those with small but finite angular momentum (figure 3*a*) display quasi-elliptical paths passing very close to the trap centre, and whose major axis tends to precess, while those with larger angular momentum can display quasi-circular orbits, a segment of which is shown in figure 3(*b*).

Careful preparation of the initial condition can lead to a nearly one-dimensional trajectory, as in figure 4(*a*) (see also supplementary movie 1 available at journals.cambridge.org/flm). Figure 4(*b*) shows the drop position and velocity as functions of time in a coordinate system aligned with the long direction of the orbit, illustrating the gradual damping of the oscillations as energy is lost to drag. The typical scales of the measured velocities v and accelerations a are consistent with but are somewhat higher than those observed previously (Linke *et al.* 2006; Lagubeau *et al.* 2011). For the range of drop radii observed, the measured accelerations correspond to forces reaching 100 μN, also consistent with previous observations. Plotting the acceleration as a function of distance from the trap centre (figure 4*c*) we see that at early times, when the drop is far from the centre, it is approximately constant. As the orbit draws closer to the origin, there is an approximately linear dependence with a slope that slowly increases with time. A phase portrait in the a, v-plane (figure 4*d*) shows a linear relationship at early times followed by the more familiar circular trajectories of a harmonic oscillator. From the theorem of Bertrand (1873), the only central force

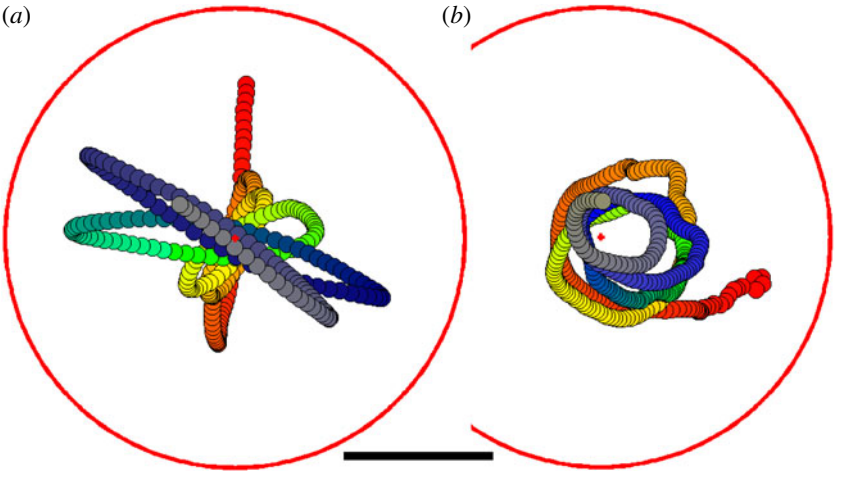

FIGURE 3. Examples of orbits. Trajectories are colour-coded by time, from red to grey, marking drop position every 15 ms. Red cross is the trap centre; large red circle indicates the outer edge of the trap. Orbits with (*a*) small and (*b*) large initial orbital angular momentum. Scale is 5 cm.

laws supporting closed orbits have the radial dependence r^{α}, with $\alpha = -2$ or 1, so the observed precession in figure 3(*a*), especially for large orbits, probably reflects the deviation of the force law from the ideal harmonic oscillator. We discuss these results further in § 4.

Among the most salient features that distinguish a Leidenfrost drop from a Leidenfrost solid such as dry ice (Lagubeau *et al.* 2011) is the excitation of persistent harmonic shape deformations as it spirals towards its final resting place. These deformations are seen only when the drop initially has large orbital angular momentum, and as the drop shrinks its spinning rate increases and the number of lobes decreases. We have observed drops with five-, four-, three-, and then two-armed shapes, some of which are shown in figure 5. Although the coexistence of multiple modes of shape oscillations on large drops makes it difficult to discern a direction of rotation, when a drop has shrunk to a size that supports only the two-lobed (dumbbell) shape its 'spin' angular momentum is clearly evident, and is always antiparallel to the orbital angular momentum. This antiparallelism can be understood as a simple consequence of launching an extended body (a drop) with uniform velocity tangential to the circular ridges and acted upon by a central force. In the two-lobed state we observe a rapid increase in spinning rate, presumably as a consequence of the shrinkage of its moment of inertia. However, we have not been able to rule out the possibility that this effect is partially due to viscous torques imparted by the ratchet and flows internal to the drop.

As a dumbbell-shaped drop continues to shrink and its angular speed increases it invariably undergoes binary fission, often with the classical satellite drop visible from the breakup of the connecting thread of fluid (figure 6 and supplementary movie 2). The balance of centripetal and capillary forces for a drop rotating at angular velocity Ω about its centre of mass is governed by the rotational Bond number

$$\Sigma = \frac{\Delta\rho\Omega^2 r_0^3}{8\sigma}, \tag{2.1}$$

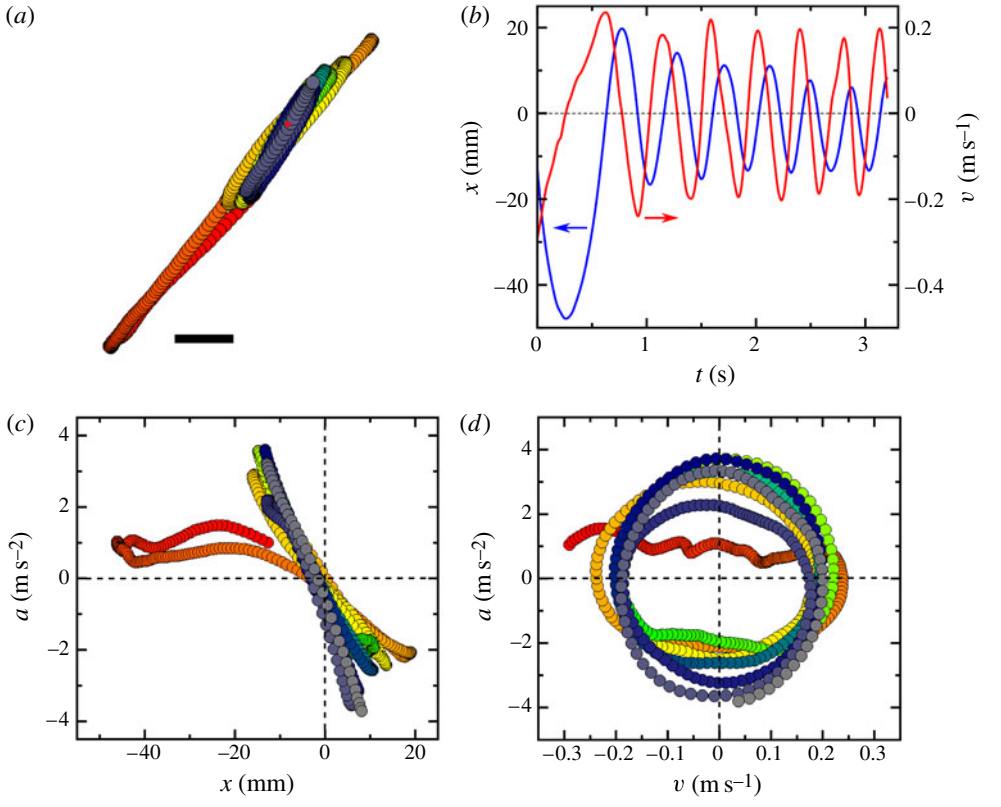

FIGURE 4. Analysis of a quasi-one-dimensional orbit. (*a*) Orbit colour-coded as in figure 3. Scale is 1 cm. See supplementary movie 1. (*b*) Temporal evolution of position (blue) and velocity (red) of the trajectory in (*a*), in a coordinate system rotated to lie along the major axis of the orbit. Acceleration versus (*c*) position and (*d*) velocity, with the same colour scheme as (*a*).

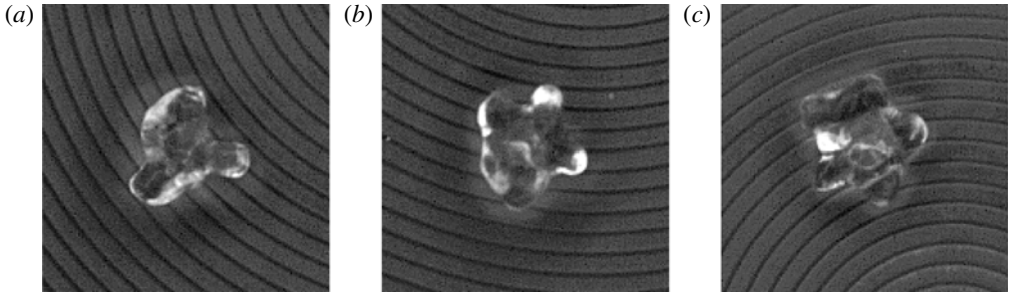

FIGURE 5. Modes of orbiting Leidenfrost drops. (*a*)–(*c*) 3-, 4-, and 5-lobed drops.

where $\Delta\rho$ is the density difference between the drop fluid and the surrounding vapour, r_0 is the radius of a spherical drop with the same volume, and σ is the surface tension (Chandrasekhar 1965; Brown & Scriven 1980). Calculations of the stability of ellipsoidal figures of equilibrium indicate a critical value $\Sigma^* \simeq 0.30$ for the point of subcritical bifurcation to a two-lobed shape from the axisymmetric one. These shapes

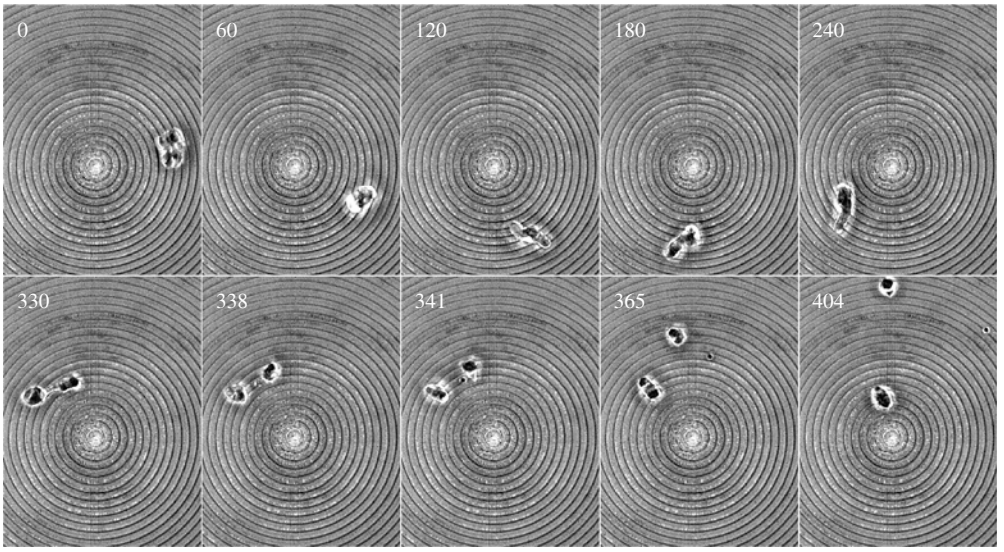

FIGURE 6. Binary fission of a Leidenfrost drop. Times (in ms) from the first frame are indicated. The drop displays dumbbell-shaped oscillations as it orbits, eventually splitting in two with the creation of a small satellite drop. See supplementary movies 2 and 3.

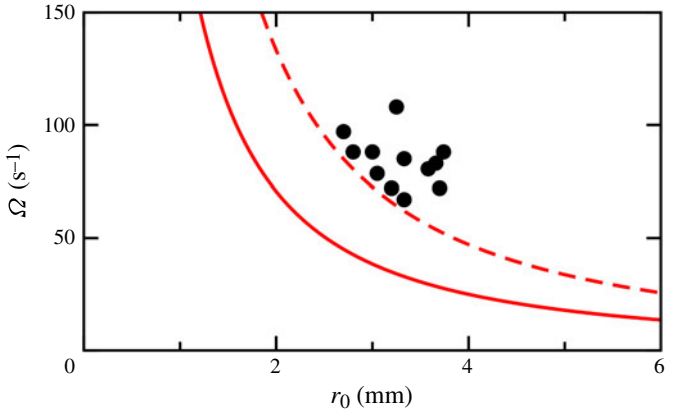

FIGURE 7. Data on drop fission. Measured spinning frequency versus equivalent drop radius (solid circles), compared to theoretical criteria for an $n = 2$ bifurcation (dashed red curve) and the stability limit for a two-lobed shape (solid red curve).

exist along a stable branch down to $\Sigma^{\dagger} = 0.09$. In the context considered here, there is a slow variation in Σ with time as the drop shrinks and spins faster, so any crossing of these bifurcation values is an example of a 'dynamic bifurcation' of the kind studied in celestial mechanics (Lebovitz & Pesci 1995). Our experimental study of 12 fission events imaged at 1000 f.p.s. shows that drops appear to be unstable to fission as soon as they become visibly two-lobed, executing very few rotations before breaking up. In figure 7 we plot the measured angular frequency Ω during the first full rotation after the appearance of the two-lobed shape, hence just before fission, as a function of the equivalent radius of the drop. These data are compared to the theoretical

onset curves using Σ^* and $\Sigma^\dagger$ which together define the theoretical stability limits for non-axisymmetric drops. Our data cluster near but above the bifurcation curve defined by Σ^*, consistent with our observation that once the drops develop the 2-lobed shape they are unstable to breakup. This is perhaps not surprising because, unlike in the theoretical calculations, the Leidenfrost drops are undergoing destabilising, large-amplitude shape oscillations. Finally, we should remark that one can even find examples of breakup and subsequent merger of the two daughter drops (supplemental movie 3).

3. Ratchet mechanism

Above a smooth, flat heated solid a Leidenfrost drop is levitated by the vapour flow from its bottom surface, which exits the gap between the drop and the underlying surface uniformly in all directions. If the diameter of the drop exceeds the capillary length $\ell_c = (\sigma/\rho_l g)^{1/2}$, where σ is the liquid–air surface tension, ρ_l is the liquid density, and g is the acceleration due to gravity, the drop's height is approximately $2\ell_c$ (Biance, Clanet & Quéré 2003) and the gap d between the drop and the surface is approximately uniform in thickness provided the typical lateral dimension does not greatly exceed ℓ_c (Myers & Charpin 2009). We shall focus on this regime of wide, flattened drops. To estimate the downward velocity v_d of the vapour emanating from the drop, assume a drop of radius R, height $2\ell_c$, with a lifetime τ. A rough estimate of the volumetric vapour production rate is $\beta 2\pi R^2 \ell_c/\tau$, where $\beta = \rho_l/\rho_v$ is the ratio of liquid to vapour densities ($\beta \sim 10^3$ for water under our experimental conditions). Assuming that this production is uniform over the bottom surface of the drop, then $v_d = 2\beta\ell_c/\tau \sim 4/\tau$ m s^{-1}. Because this evaporative flux exits the ribbon-shaped periphery of the cylindrical volume under the drop, with area $2\pi Rd$, then by flux conservation the mean velocity of the outflow is $v_m = (R/2d)v_d = \beta\ell_c R/(\tau d) \sim 1000/\tau$ for typical values of $R \sim 5$ mm and $d \sim 0.1$ mm. The associated Reynolds number in the gap is then $Re = v_m d/\nu_v = \beta\ell_c R/\tau\nu_v$, where ν_v is the kinematic viscosity of the vapour, estimated as that at the midpoint temperature in the gap. The lifetime of the drop on smooth surfaces can reach 500 s (Biance *et al.* 2003), in which case $v_d \sim 5$ mm s^{-1} and $Re \sim 1$, while in our experiments the lifetime $\tau \sim 10$–15 s, implying $v_d \sim 30$–40 cm s^{-1} and hence Re can reach $\mathcal{O}(10^2)$. This underlies the argument (Lagubeau *et al.* 2011) that the propulsion could be understood as an inertial effect akin to that of a rocket with mass loss, rather than a viscous mechanism related to drop deformations proposed by Linke *et al.* (2006). Indeed, Lagubeau *et al.* (2011) have elegantly shown that directed motion on a ratchet also occurs for dry-ice discs, so drop deformations are not necessary for propulsion. In order to examine these proposals, we investigate this problem using direct numerical solutions of the Navier–Stokes equations for a simplified model of a Leidenfrost solid over smooth and ratcheted surfaces.

This model ignores the detailed thermal processes involved in evaporation and levitation, and consists of a rigid disc of radius R and height h, surrounded by air. The disc bottom is a uniform source of air exiting downward at velocity v_d, held a distance d above a no-slip surface. As we are interested in the motion of either a Leidenfrost solid or a drop whose viscosity greatly exceeds that of the air, we also assume no-slip boundary conditions on the disc, thereby ignoring in the case of a drop any internal motions that might be driven by viscous or thermocapillary stresses. Numerical solution of this problem was performed with a commercial finite-element code (Comsol) in physical units, exploiting reflection symmetry to solve

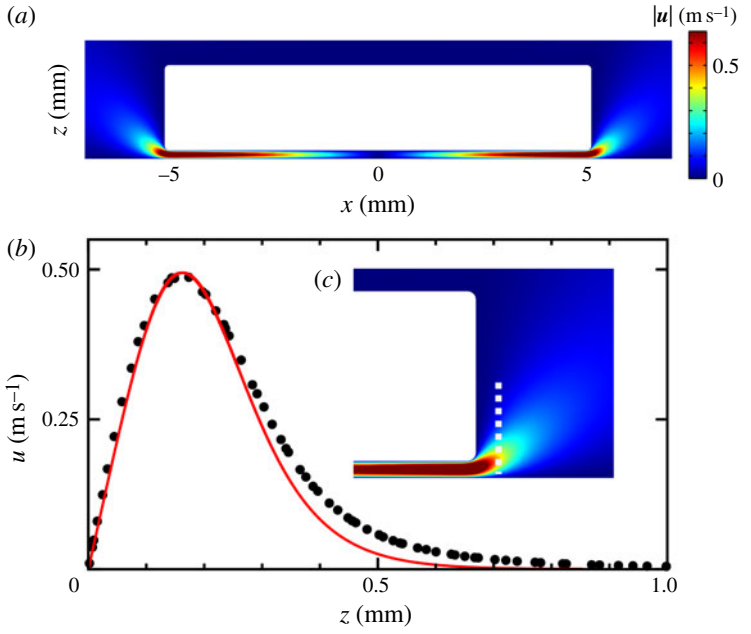

FIGURE 8. Numerical results for two-dimensional vapour flow around a Leidenfrost solid above a flat surface. (*a*) Velocity magnitude showing wall jets emanating from the gap ends. (*b*) Numerical horizontal velocity component (circles) as a function of distance from the bottom surface along the dotted line indicated in (*c*) compared with analytical results (red line).

in a semicircular domain above a ratchet topography, or exploiting radial symmetry above a flat surface to reduce the system to two dimensions. We use a vapour density $\rho_v = 1$ kg m^{-3} and viscosity $\mu = 3 \times 10^{-5}$ Pa s appropriate for air at 200 °C. Figure 8(*a*) illustrates results for the case $R = 5$ mm, $h = 2$ mm and a downward velocity of $v_d = 0.03$ m s^{-1} that is at the lower end of what would be estimated from the drop lifetime in our experiments. In keeping with the Reynolds number estimated above, the flow escaping from the ends of the gap below the solid forms well-defined jets. The vertical edge of the solid and the flat surface act as nozzle walls, which with the exiting gap flow constitutes the classic geometry of a wall jet. This observation is supported by the comparison in figure 8(*b*) between the numerical values of the horizontal velocity as a function of height above the plane and the analytical results for the self-similar wall jet (Glauert 1956), where a virtual origin and jet constant were chosen to match the value and location of the peak velocity. While the momentum flux of this jet is large, it does not imply a significant force acting on the disc for, unlike with the propulsion of a rocket, there is no surface of the disc whose normal is collinear with the direction of that flux. If we draw a control surface tightly around the disc we see that horizontal forces will arise from the weak pressure gradient acting on the vertical walls due to diffusion of the wall jet. These pressure forces are dominated by the viscous tractions acting on the disc bottom.

In the simulations described below, we shall see that airflow over a ratchet topography, even in the absence of drop deformations, is primarily directed laterally out from under the solid, guided by the channels formed by the teeth walls and the disc bottom, except at the front and back teeth. There is no appreciable flow between channels. Within any given interior channel, the influx of vapour from the

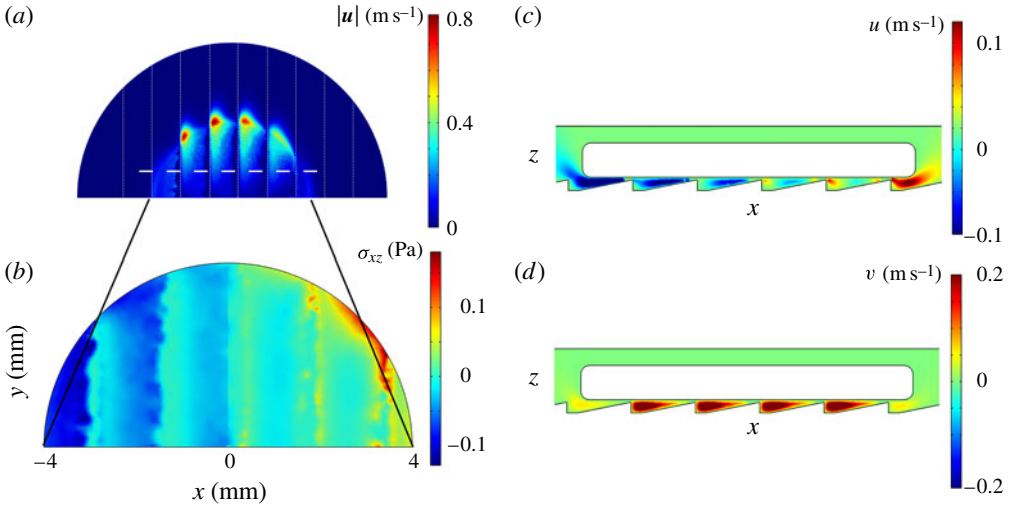

FIGURE 9. Numerical results for airflow over a ratchet. (*a*) Magnitude of the velocity in a plane between the disc bottom and the top of the ratchet teeth. (*b*) Component of in-plane viscous stress in the x-direction. (*c*) Longitudinal and (*d*) transverse velocity components in a vertical slice as indicated by the white dashed line in (*a*).

drop is diverted first forward towards the widest section of the channel, and then outward, hugging the vertical wall. This first flow results in a large viscous force pulling the drop forward, towards the vertical faces of the ratchet. To illustrate these conclusions, figure 9 shows numerical results for a disc of radius $R = 4$ mm, v_d as above, at a height $d = 0.06$ mm above the top of the teeth of a ratchet with dimensions $\lambda = 1.5$ mm and $\delta = 0.3$ mm. For these computations the finite-element grid was chosen to allow typically 5–10 mesh points across the depth of a tooth, with geometry-based refinement near tooth and disc corners. Figure 9(*a*) shows the magnitude of the vapour velocity in a plane in the middle of the gap between the teeth tops and the disc bottom, showing the laterally deflected airflow and that the maximum in the outflow velocity is at the deepest part of each channel. In figure 9(*c*) we observe that the largest values of the leftward (negative) component u of the velocity occur in the narrowest regions of each triangular channel, while the largest values of the lateral component v are found in the deepest regions (figure 9*d*). In addition, as with the smooth substrate, there are wall jets emanating from the front and rear of the disc, but now in slightly different directions; the rightward jet in figure 9(*c*) is parallel to the shallow slope of the ratchet teeth, while the leftward jet is deflected upward. Figure 9(*b*) shows the x-component of the viscous stress on the disc bottom. The colour scheme shows that this stress is large and leftward at the left edge of the drop where the air exits relatively unimpeded, and it is also large and leftward within each interior channel. The only exceptions are the rear two channels, which by virtue of being mostly open allow backwards flow. This is a similar mechanism to that proposed by Linke *et al.* (2006) but does not require drop deformations. For the small value of v_d used, the scale of stresses is Pa (=μN mm^{-2}), so for short-lived droplets with much higher rates of evaporation we expect forces in the range of 10–100 μN, as observed.

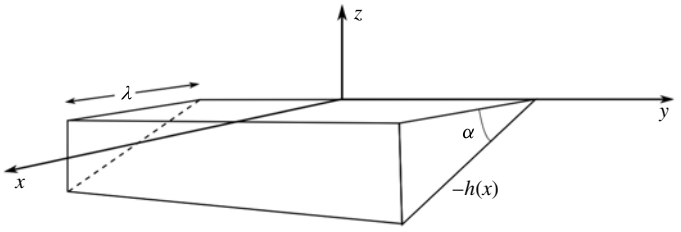

FIGURE 10. Schematic of the triangular channel below a drop.

It is possible to obtain an approximate value of the net force on the drop by calculating, within the lubrication approximation, the flow inside a triangular channel. Consider the geometry of figure 10, for $-h(x) \leqslant z \leqslant 0$ with $h = x\tan\alpha$, where α is the angle of the sloped channel wall. If $\boldsymbol{u} = (\boldsymbol{u}_H, w)$ is the velocity of the vapour in the channel, where $\boldsymbol{u}_H$ is the velocity on the x, y-plane, and p is the pressure, then

$$\boldsymbol{u}_H = -\frac{1}{2\mu}\boldsymbol{\nabla}_\perp pz(z+h). \tag{3.1}$$

Invoking continuity, an expression is found for the vertical component w of the velocity, with boundary conditions $w|_{z=0} = -v_d$ and $w|_{z=-h} = 0$. This second boundary condition yields a two-dimensional Poisson equation for the pressure field

$$\nabla_\perp^2 p = \frac{12\mu v_d}{h^3}. \tag{3.2}$$

This equation has a similarity solution for the case of a semi-infinite triangular wedge. Even though we would not expect this to be globally valid in the present case, it is still possible to make use of this solution because the largest contribution to the stress occurs in the narrowest region of the channel. Within this approximation $p = (6\mu v_d/\tan^2\alpha)x^{-1}f(\eta)$, where $\eta = y/x$ and

$$f(\eta) = \frac{\eta^2 + A\eta + B}{\eta^2 + 1}. \tag{3.3}$$

Here, $A = 0$ by symmetry and B is chosen to satisfy mass conservation. Replacing p into (3.1) we obtain the velocity field, the approximate value of the stress tensor at $z = 0$, and the viscous drag due to the flow inside a given tooth of length $2R$ and width λ that is separated from the drop by a minimum gap e,

$$\boldsymbol{F} \simeq \hat{\boldsymbol{x}}\frac{3\mu v_d R}{\tan^2\alpha}\left[1 + \ln\left(\frac{\lambda}{2e}\right)\right] + O\left(\frac{\lambda}{R}\right)^2. \tag{3.4}$$

Note that the component of the drag force parallel to the ratchet ridges will cancel out by symmetry, leaving only the component perpendicular to the ridges. Recognising that $\tan\alpha = h/\lambda$ and that by continuity the characteristic horizontal velocity u_0 in the gap is $u_0 \sim v_d\lambda/h$, we conclude that the propulsive force per tooth is $\boldsymbol{F} \sim \hat{\boldsymbol{x}}\mu u_0 R\lambda/h$, in agreement with Dupeux *et al.* (2011*b*). Multiplying this result by the number of teeth, R/λ, we conclude that the total propulsive force on the drop should scale as R^2/h. Using the known scaling $h \sim R^{1/2}$ for the mean levitation height (Biance *et al.* 2003), we obtain the scaling $F \sim R^{3/2}$ observed by Lagubeau *et al.* (2011). The substitution of typical parameter values into (3.4) yields a drag force of approximately 20 μN, in good agreement with the experimental results (Lagubeau *et al.* 2011). Of

course, the magnitude of this force will vary with time as the drop radius and levitation height change. Finally, it should also be pointed out that the presence of curvature in the ratchet would only accentuate the rectification of the flow and the consequent excess viscous force in the direction of the steep side of the ridges, i.e. towards the centre of the trap.

In addition to the central force described above, a solid disc moving with speed U experiences a viscous drag force $F_v \sim \pi R^2 \mu U/d$ associated with the thin vapour layer underneath, and an aerodynamic drag $F_a \sim \rho_v U^2 4\ell_c R C_D$ due to the motion of the drop through the air, where C_D is the drag coefficient which depends on the Reynolds number Re_d of the moving drop. For U of the order of 0.1 m s^{-1}, $Re_d \sim 10$, and $C_D \sim O(1)$ (Schlichting 1968). The ratio of these two forces takes the form of a Reynolds number, $F_a/F_v \sim U(\ell_c d/R)C_D/\nu_a \sim 0.1$ s m^{-1}U. Given that the maximum drop speeds observed in our experiments are 0.2 m s^{-1}, the aerodynamic drag is clearly a secondary effect (Lagubeau *et al.* 2011). Owing to the ratchet geometry, the component of the drag parallel to the ridges is inversely proportional to the mean vapour layer depth $d/2$. On the other hand, the calculation above suggests that the radial drag is dominated by a contribution logarithmic in the narrowest dimension e. In addition to this anisotropy, recent work has shown that deformable (liquid) drops are subjected to other mechanisms of viscous dissipation (Dupeux *et al.* 2011*a*). We conclude that the drag force on a Leidenfrost drop is anisotropic, with two different drag coefficients ζ_r and ζ_θ.

4. Droplet motion in a trap

Within the model of a centrally directed force of magnitude $F(t)$ acting on the drop, its equation of motion resembles that of a celestial body (Symon 1971) with the added feature of viscous drag. If a drop of mass $M(t)$ is located at $\boldsymbol{r}(r,\theta) = r\hat{\boldsymbol{r}}$ with $(\hat{\boldsymbol{r}}, \hat{\boldsymbol{\theta}})$ the local orthogonal system (figure 1), then a force balance yields

$$\ddot{r} - r\dot{\theta}^2 = -\Gamma - b_r\dot{r}, \tag{4.1a}$$

$$r\ddot{\theta} + 2\dot{r}\dot{\theta} = -b_\theta r\dot{\theta}. \tag{4.1b}$$

where $\Gamma = F/M$, and each of the drag coefficients ζ, or equivalently the rates $b_i = \zeta_i/M$ $(i = r, \theta)$, may depend on time owing to the changing drop size and vapour cushion thickness. Integration of (4.1*b*) shows the conservation of $L_0 = \exp(f_\theta(t))r^2\dot{\theta}$, where $f_i(t) = \int_0^t b_i(t')\,\mathrm{d}t'$. Substituting into (4.1*b*) we obtain

$$\ddot{r} + b_r\dot{r} - L_0^2\frac{\mathrm{e}^{-2f_\theta(t)}}{r^3} = -\Gamma(t). \tag{4.2}$$

To the extent that Γ is at most slowly varying with time, there are two interesting regimes in which there is a separation of time scales such that the drop properties change slowly through each orbit. First, when a drop is launched into an orbit of radius R_0 with an initial angular momentum corresponding to an orbital frequency $\omega = (\Gamma/R_0)^{1/2}$, and the damping is such that $b_\theta/\omega \ll 1$, then $\ddot{r}$ and $\dot{r}$ can be neglected, and an approximate solution to (4.2) is a quasi-circular spiralling orbit,

$$r(t) = R_0\mathrm{e}^{-(2/3)b_\theta t}, \quad \theta(t) = \frac{3\omega}{b_\theta}\mathrm{e}^{(1/3)b_\theta t} + \theta_0, \tag{4.3}$$

qualitatively similar to figure 3(*b*). This approximation improves as time increases, since the neglected terms decay exponentially with respect to the others.

In the second case, $L_0 = 0$ and the problem is one-dimensional (say, along x), with

$$\frac{\mathrm{d}v}{\mathrm{d}t} + b_r v = \mp|\Gamma|, \quad v = \frac{\mathrm{d}x}{\mathrm{d}t}, \tag{4.4}$$

where $\mp$ is introduced to account for the ratchet force always being toward the origin. The full trajectory is composed of successive segments on either side of the origin. In any one segment the formal solution is

$$x(t) = \mp \int^{t} \mathrm{e}^{-f_r(t')} \int^{t'} \mathrm{e}^{f_r(s)} |\Gamma(s)| \, \mathrm{d}s \, \mathrm{d}t', \tag{4.5}$$

where $\mp$ refers to $x \gtrless 0$. A particularly simple limit occurs when the lifetime of the drop is large compared to the duration of two successive legs, and the coefficients in (4.4) can be assumed constant. Starting from the origin and moving to the right the particle will have a turning point at $b_r x_m = v_0 - v_L \ln[1 + (v_0/v_L)]$ at time $b_r t_m = \ln[1 + (v_0/v_L)]$, and will return to the origin at time $t_m + t_0$ where $b_r t_0 - \exp(-b_r t_0) = b_r x_m / v_L - 1$ with a final velocity $v_f = -v_0 + v_L b_r t_0 + v_L \ln[1 + (v_0/v_L)]$, where $v_L = \Gamma / b_r$. This analysis allows one to determine Γ and b_r from measurements of the velocity over one cycle.

The theoretical results corresponding to trajectories with initial angular momentum can lead to decaying, precessing orbits like those seen at early times in figure 3(*a*). However, the later behaviour observed, in which the orbital extent transiently increases, is a first clear indication that there is a qualitative change in the nature of the force F. Another indication is seen in the analysis of quasi-linear trajectories (figure 4*a*), in which at later times the phase plane orbits are circular instead of the piecewise linear form predicted by (4.4) for constant $|\Gamma|$. Because these departures from the simplest model occur for cases when the drop crosses very near to the trap centre, it is natural to infer that the sudden reversal of direction is responsible for the effect. Note that the vortical flows inside the drop created by the viscous drag on its bottom surface will tend to reverse direction as the drop crosses the trap centre; the time to re-establish the flow is $(h/2)^2 / \mu_l$, where μ_l is the fluid viscosity. For water drops this time is $\sim$1 s, comparable to the oscillation period, indicating that the internal dynamics cannot be neglected.

In summary, we have shown that a circular ratchet trap is able to induce a variety of complex trajectories of Leidenfrost drops, and have presented theoretical and computational evidence that the fundamental ratchet mechanism is viscous in origin and does not require drop deformations. This therefore reconciles the apparent contradiction between the viscous mechanism for liquid drops proposed by Linke *et al.* (2006) and the propulsion of rigid dry-ice discs observed by Lagubeau *et al.* (2011). Nevertheless, as drops move over the ratchet they do display deformations and complex internal dynamics such as fission and fusion, and these are worthy of further study at both the macroscopic and microscopic scales (Ok *et al.* 2011).

Acknowledgements

As this work was nearing completion we learned of the work of Dupeux *et al.* (2011*b*), which reaches similar conclusions about the viscous mechanism of drop motion. We are grateful to D. Quéré for the communication of these unpublished results. The authors thank J. R. Lister and T. J. Pedley for important discussions, and D. Page-Croft and N. Price for technical assistance. This work was supported in part by the Schlumberger Chair Fund and NSF Grant 0965248 (J.W.J.).

Supplementary movies are available at journals.cambridge.org/flm.

REFERENCES

ADACHI, K. & TAKAKI, R. 1984 Vibration of a flattened drop. Part 1. Observation. *J. Phys. Soc. Japan* **53**, 4184–4191.

BERTRAND, J. 1873 Théorème relatif au mouvement d'un point attiré vers un centre fixe. *C. R. Acad. Sci.* **77**, 849–853.

BIANCE, A.-L, CLANET, C. & QUÉRÉ, D. 2003 Leidenfrost drops. *Phys. Fluids* **15**, 1632–1637.

BROWN, R. A. & SCRIVEN, L. E. 1980 The shape and stability of rotating liquid drops. *Proc. R. Soc. Lond.* A **371**, 331–357.

CHANDRASEKHAR, S. 1965 The stability of a rotating fluid drop. *Proc. R. Soc. Lond.* A **286**, 1–26.

DUPEUX, G., LE MERRER, M., CLANET, C. & QUÉRÉ, D. 2011*a* Trapping Leidenfrost drops with crenelations. *Phys. Rev. Lett.* **107**, 114503.

DUPEUX, G., LE MERRER, M., LAGUBEAU, G., CLANET, C., HARDT, S. & QUÉRÉ, D. 2011*b* Viscous mechanism for Leidenfrost propulsion on a ratchet. *Europhys. Lett.* **96**, 58001.

GLAUERT, M. B. 1956 The wall jet. *J. Fluid Mech.* **1**, 625–643.

LAGUBEAU, G., LE MERRER, M., CLANET, C. & QUÉRÉ, D. 2011 Leidenfrost on a ratchet. *Nat. Phys.* **7**, 395–398.

LEBOVITZ, N. R. & PESCI, A. I. 1995 Dynamic bifurcation in Hamiltonian systems with one degree of freedom. *SIAM J. Appl. Maths* **55**, 1117–1133.

LEIDENFROST, J. G. 1756 *De Aquae Communis Nonnullis Qualitatibus Tractatus*. Herman Ovenius.

LINKE, H., ALEMÁN, B. J., MELLING, L. D., TAORMINA, M. J., FRANCIS, M. J., DOW-HYGELUND, C. C., NARAYANAN, V., TAYLOR, R. P. & STOUT, A. 2006 Self-propelled Leidenfrost droplets. *Phys. Rev. Lett.* **96**, 154502.

MYERS, T. G. & CHARPIN, J. P. F. 2009 A mathematical model of the Leidenfrost effect on an axisymmetric droplet. *Phys. Fluids* **21**, 063101.

OK, J. T., LOPEZ-OÑA, E., NIKITOPOULOS, D. E., WONG, H. & PARK, S. 2011 Propulsion of droplets on micro- and sub-micron ratchet surfaces in the Leidenfrost temperature regime. *Microfluid. Nanofluid.* **10**, 1045–1054.

SCHLICHTING, H. 1968 *Boundary-Layer Theory*, 6th edn. McGraw-Hill.

SYMON, K. R. 1971 *Mechanics*, 3rd edn. Addison-Wesley.